

Nonlinear Micromechanical Modelling of Transverse Tensile Damage Behavior in Fiber-Reinforced Polymer Composites

Nian Li*

College of Mechanical and Power Engineering, Nanjing Tech University, Nanjing, 211816, China

*Corresponding Author: Nian Li. Email: linian@njtech.edu.cn

Abstract: The investigation focusing on the mechanical behaviors at the micro-structural level in composite materials can provide valuable insight into the failure mechanisms at larger scales. A micromechanics damage model which comprises the coupling of the matrix constitutive model and the cohesive zone (CZM) model at fiber-matrix interfaces is presented to evaluate the transverse tensile damage behaviors of unidirectional (UD) fiber-reinforced polymer (FRP) composites. For the polymeric matrix that exhibits highly non-linear mechanical responses, special focus is paid on the formulation of the constitutive model, which characterizes a mixture of elasticity, plasticity as well as damage. The proposed constitutive model includes the numerical implementation of a fracture plane based ellipse-parabola criterion that is an extension of the classic Mohr-Coulomb criterion, corresponding post-yield flow rule and post-failure degradation rule in the fully implicit integration scheme. The numerical results are in good agreement with experimental measurements. It is found that directly using the matrix properties measured at the ply level to characterize the mechanical responses at the constituent level may bring large discrepancies in homogenized stress-strain responses and dominant failure mechanisms. The distribution of fracture plane angles in matrix is predicted, where it is shown to provide novel insight into the microscopic damage initiation and accumulation under transverse tension.

Keywords: Fracture plane angle; elasto-plasticity; damage; micromechanical model; polymer matrix composites

1 Introduction

The potential of composite materials in providing high stiffness and strength in lightweight structural components is governed by adequate understanding of complex failure mechanisms that initiate at the microscopic scale. Throughout the years, physically-based failure criteria have been widely developed to characterize damage behaviors in fiber-reinforced polymer (FRP) composite materials under various loading conditions. However, owing to high complexity of failure mechanisms and uncertainty during manufacturing process, the existing failure theories still remain controversies and challenges. The well-recognized Puck's failure criterion [1], which has been reported as one of the most predictive criterion in the World-Wide Failure Exercises (WWFE), still does not achieve good performances for all generic loading conditions [2, 3]. In particular for tri-axial loading cases, significant difference between predictions and experimental data could be observed, which is probably attributed to the lack of

appropriate consideration of the localized fiber-matrix failure interaction at the micro-scale. Moreover, most of criteria are dependent on specific empirical parameters, of which the values are hardly measured by experimental methods and needs to be determined by introducing artificial hypothesis. For instance, the inclination parameters in the Puck's failure criteria is actually estimated by the fracture envelop of stress combinations under the simple material principal axis coordinate, i.e., (σ_2, τ_{12}) , rather than the stress combinations acting on the fracture plane, i.e., (σ_n, τ_{nl}) . This assumption regards composite materials as completely brittle materials which is intrinsically with the fracture angle of 0° under pure tension and the fracture angle of 45° subjected to pure shear stress. However, since inter-fiber fracture (IFF) is dominated by matrix and interface properties, some types of GFRP/Epoxy and CFRP/Epoxy might not be intrinsically brittle [4]. Thus to some extent the Puck failure criterion lacks rationality and does not perform so well in certain loading cases.

In order to eliminate experimentally inaccessible or empirical parameters associated with the formulation of the failure theory, interactive stress-based failure criteria, following Mohr's fracture hypothesis, are proposed by the author [5]. In contrast to other criteria, the fracture angles under uniaxial stress states, like basic strengths, are employed as known parameters, because only by both the fracture angle and failure stresses, can Mohr's hypothesis be described faithfully and completely. But unfortunately, the experimental results of fracture angles for transverse loading scatter considerably by existing test methods, and may be influenced strongly by ductile or brittle natures of materials.

On a real-world structural level, whole components with complex geometry are regarded. The local state of stress at an arbitrary position are provided within the component that are built up of FRP composite laminates, due to the external load applied. Thus, in order to finally predict structural strength, it seems quite reasonable to firstly analyze failure mechanisms in a UD lamina, since laminates can be considered as a set of lamina. Experimental observations have demonstrated that fiber tensile damage, fiber compressive damage, matrix tensile damage (i.e., transverse tensile damage) and matrix compressive damage are the four dominant intralaminar failure modes on the lamina level (or the meso-scale level) [4]. In fact, a sequence of multiple failure events occurring are dictated by micro-damage of different phases, e.g., microscopic matrix cracks and local fiber-matrix debonding. Hence, micromechanical analysis may be a promising way to determine the failure angles under transverse loads, and meanwhile gives its detailed insight of the composite failure mechanisms by considering the influence of each constituent. A variety of constitutive models [6-13] have been developed to model the nonlinear micro-mechanical response of composites. In general, the elasto-plastic behavior of epoxy matrix is modelled using Mohr-Coulomb yield criteria (or extended Drucker-Prager yield criteria). However, it should be noticed that although they employ the concept of stresses on the fracture surface, they do not identify the orientation of the fracture surface. Some predicted results might be incorrect in some cases, such as the uniaxial tensile test for cast iron [14], probably due to a simplest linear equation suggested by Coulomb.

The subject of the present work is to propose a micromechanical model, consisting of matrix, fibers and fiber-matrix interfaces, to predict the mechanical behaviors and the fracture angles of composites in transverse loading cases, within the framework of Mohr's fracture hypothesis. In particular, this work focuses on the numerical implementation of an elasto-plastic with damage constitutive model for epoxy matrix, based on the modified yield (or failure) criteria, inspired by the fracture plane ideas of Mohr and Coulomb, for isotropic materials. Parametric analyses, including the effect of constituent material and fiber-matrix interface properties on the homogenized responses of representative volume elements (RVEs), will be also carried out. The results including homogenized behaviors, damage scenarios and fracture plane angles, are compared to the uniaxial tensile experiments to validate the micromechanical model presented in this paper.

2 Constitutive Modeling

The formulation of the constitutive model therefore naturally takes into account three individual components including the reinforcing fibers, the polymeric matrix and the fiber-matrix interface. The fibers are treated as linearly elastic and transversally isotropic. Interfacial debonding is simulated, using zero-thickness cohesive elements at the interface between fiber and matrix region, with a bilinear traction-separation law. The initiation of debonding is captured by a quadratic interaction criterion of the interface strength for various interlaminar fracture modes, while the subsequent propagation is governed by the energy-based B-K propagation criterion that evaluates the fracture energy dissipation on mixed-mode fracture. Since the epoxy matrix plays a crucial role in the cracking formation and the nonlinear response of the ply subjected to transverse loading, special focus therefore needs to be paid to the accurate simulation of the matrix with elasto-plastic and isotropic damage constitutive behaviors.

2.1 Modified Yield Criterion Based on Mohr's Fracture Plane Hypothesis

It is not possible to neglect the effect of hydrostatic pressure on the yielding behavior of polymers. A significant pressure-dependent isotropic yield criterion is that of Mohr-Coulomb (M-C). It, following Mohr's failure theory, states that yielding would be exclusively induced by the stresses acting on a certain plane with highest risk of failure, and has been frequently used in plasticity modeling of polymeric matrix [6-11]. Nevertheless, due to a linear expression, it indicates that the fracture angle of 0° , which would actually occur in some cases, e.g., the uniaxial tensile test for cast iron, cannot be predicted by the M-C criterion. In addition, even though the concept of the failure plane is employed, the M-C criterion does not identify the plane orientation. To resolve the contradiction, an ellipse-parabola function of Mohr's envelope, originally proposed by Chen et al. [14], is developed to formulate isotropic plasticity from the standpoint of numerical implementation. Their fracture plane based criterion has been developed and successfully proven its predictive capability in estimating fracture strength for both ductile and brittle materials, but it is not convenient for numerical implementation because of the sharp point on the failure surface. It should be noted from Fig. 1a that the deviatoric section of the corresponding yield (failure) surface is a hexagon with six sharp vertices at the Lode angle $\theta_\sigma = \pm 30^\circ$. These gradient discontinuities will result in difficulties for numerical convergence. Hence a trigonometric rounding approach is described to eliminate all apex singularities from the function with the deviatoric plane. First, the stress exposure, f_E , is rearranged to form a homogeneous function in terms of the basic stress invariants in the cylindrical coordinate system as

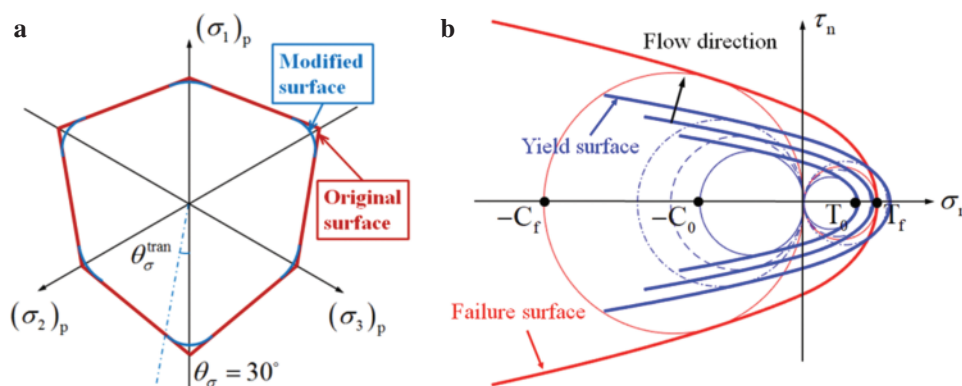


Figure 1: (a) Smooth treatment for the failure criterion in the deviatoric plane and (b) evolution of the yield surface for isotropic hardening

$$f_E(\sigma_V, \sqrt{J_2}, \theta_\sigma, \varphi) = \sqrt{(R\mu^2 + \omega\xi^2)J_2 + R\sigma_V^2 + 2R\mu\sigma_V\sqrt{J_2}} + \frac{\alpha}{2}(\sigma_V + \mu\sqrt{J_2}) \quad (1)$$

$$\text{with } R = \frac{\alpha^2}{4} + \frac{\langle \mu\sqrt{J_2} + \sigma_V \rangle}{|\mu\sqrt{J_2} + \sigma_V|} \beta, \quad \mu(\theta_\sigma) = -\frac{\sin \theta_\sigma}{\sqrt{3}} + \cos \theta_\sigma \cos 2\varphi \text{ and } \xi(\theta_\sigma) = \cos \theta_\sigma \sin 2\varphi \quad (2)$$

where $\sigma_V = I_1/3$ is the hydrostatic stress; $\bar{\sigma} = J_2$ is the second invariant of deviator stress tensor; θ_σ and φ are the Lode angle and the angle of the action plane, respectively. Note that for a given stress state, φ is the only variable and represents different yield states on all potential failure planes. Failure will occur in the one sectional plane where f_E is a maximum. In other words, the calculation of the actual failure plane angle φ_{fp} turns into a search for the global maximum of f_E . An efficient numerical algorithm, namely the Golden Section Search, is used to estimate the specific value of φ_{fp} within the range $[0, 180^\circ]$, due to the lack of analytical expression of the maximum value. Given the typical failure states under uniaxial tensile, compressive and shear loading, values of parameters α , β and ω can be given by

$$\alpha \frac{C}{2} \left(\frac{\alpha}{C\omega} - 1 \right) + \omega \frac{C^2}{4} \left[1 - \left(\frac{\alpha}{C\omega} \right)^2 \right] = 1 \quad (3)$$

$$\alpha \frac{T}{2} \left[\frac{\alpha + \beta T}{(\omega - \beta)T} + 1 \right] + \beta \frac{T^2}{4} \left[\frac{\alpha + \beta T}{(\omega - \beta)T} + 1 \right]^2 + \omega \frac{T^2}{4} \left\{ 1 - \left[\frac{\alpha + \beta T}{(\omega - \beta)T} \right]^2 \right\} = 1 \quad (4)$$

$$\frac{\alpha^2}{2(\omega - \beta)} + \beta \left[\frac{\alpha}{2(\omega - \beta)} \right]^2 + \omega S^2 \left\{ 1 - \left[\frac{\alpha}{2(\omega - \beta)S} \right]^2 \right\} = 1 \quad (5)$$

where T, C and S are uniaxial tensile, compressive and shear strengths respectively. In particular, if $S = T$, Eqs. (4) and (5) no longer hold. Equations will be substituted by

$$\alpha T + \beta T^2 = 1, \quad \frac{\alpha}{2(\omega - \beta)T} = 1 \quad (6)$$

It can be observed from Fig. 1a that the deviatoric section of the corresponding failure surface is a hexagon with six sharp vertices at the Lode angle $\theta_\sigma = \pm 30^\circ$. In order to avoid difficulties for numerical convergence induced by those gradient discontinuities, a trigonometric rounding approach is described to eliminate all apex singularities from the function with the deviatoric plane. Piece-wise trigonometric approximations of both $\mu(\theta_\sigma)$ and $\xi(\theta_\sigma)$ are constructed to eliminate singular vertices and approach the original envelope as close as possible. With the employment of a specified transition angle $\theta_\sigma^{\text{tran}}$ ($0^\circ \leq \theta_\sigma^{\text{tran}} \leq 30^\circ$) near the vicinity of singularities, the forms of approximations are defined as

$$\mu(\theta_\sigma) = \begin{cases} -\frac{\sin \theta_\sigma}{\sqrt{3}} + \cos \theta_\sigma \cos 2\varphi & |\theta_\sigma| \leq \theta_\sigma^{\text{tran}} \\ A_1 - B_1 \sin 3\theta_\sigma & |\theta_\sigma| > \theta_\sigma^{\text{tran}} \end{cases}, \quad \xi(\theta_\sigma) = \begin{cases} \cos \theta_\sigma \sin 2\varphi & |\theta_\sigma| \leq \theta_\sigma^{\text{tran}} \\ A_2 - B_2 \sin 3\theta_\sigma & |\theta_\sigma| > \theta_\sigma^{\text{tran}} \end{cases} \quad (7)$$

According to the continuity and smooth conditions at the transition angle ($|\theta_\sigma| = \theta_\sigma^{\text{tran}}$), the values and gradients of $\mu(\theta_\sigma)$ and $\xi(\theta_\sigma)$ within the interval $|\theta_\sigma| \leq \theta_\sigma^{\text{tran}}$ are equal to those lying in $|\theta_\sigma| > \theta_\sigma^{\text{tran}}$. Utilizing these conditions in Eq. (7) results in

$$\begin{aligned}
A_1 &= \frac{\cos \theta_\sigma^{\text{tran}}}{3} \left[(\tan 3\theta_\sigma^{\text{tran}} \tan \theta_\sigma^{\text{tran}} + 3) \cos 2\varphi + \frac{\text{sign}(\theta_\sigma)}{\sqrt{3}} (\tan 3\theta_\sigma^{\text{tran}} - 3 \tan \theta_\sigma^{\text{tran}}) \right] \\
B_1 &= \frac{1}{3 \cos 3\theta_\sigma^{\text{tran}}} \left(\frac{\cos \theta_\sigma^{\text{tran}}}{\sqrt{3}} + \text{sign}(\theta_\sigma) \sin \theta_\sigma^{\text{tran}} \cos 2\varphi \right) \\
A_2 &= \sin 2\varphi \left(\frac{\sin 3\theta_\sigma^{\text{tran}} \sin \theta_\sigma^{\text{tran}}}{3 \cos 3\theta_\sigma^{\text{tran}}} + \cos \theta_\sigma^{\text{tran}} \right), \quad B_2 = \sin 2\varphi \frac{\text{sign}(\theta_\sigma) \sin \theta_\sigma^{\text{tran}}}{3 \cos 3\theta_\sigma^{\text{tran}}}
\end{aligned} \tag{8}$$

where $\text{sign}(\theta_\sigma)$ denotes the sign attribute of the Lode angle θ_σ . Clearly, the greater the value of $\theta_\sigma^{\text{tran}}$ is, the better fitting the original cross section is obtained. However, $\theta_\sigma^{\text{tran}}$ may not be too near 30° to avoid numerical ill-condition, hence a value of 29° is selected in practice. The original and modified yield surfaces in the deviatoric plane are plotted in Fig. 1a.

The hardening effect is defined to describe the change of stress transmitted by a yielding material as the plastic flow continues. Under the framework of the developed failure criterion, each loading surface is determined by the combination of parameters α , β and ω at an intermediate state. As shown in Fig. 1b, an isotropic hardening law is introduced by assuming that loading surfaces are similar with regard to the initial yield one. The isotropic hardening model can be constructed by keeping the ratio of hardening parameters constant during loading. And its yield surface will be cut off by the ultimate failure surface, while the one for general nonlinear hardening model does not go beyond.

A non-associated flow rule is used to specify the direction of plastic flow. The plastic potential function, g , is assumed to have the similar form as the developed yield criterion.

$$g = \sqrt{(R\mu^2 + \omega\xi^2)J_2 + R(k_p\sigma_v)^2 + 2R\mu(k_p\sigma_v)\sqrt{J_2} + \frac{\alpha}{2}(k_p\sigma_v + \mu\sqrt{J_2})} \tag{9}$$

where k_p is a material parameter allowing for a correct definition of the volumetric deformation in plasticity. It can be evaluated by a relation between the volumetric and longitudinal plastic strains under uniaxial tension. The angle of the action plane in the flow rule is set equal to the one once plastic flow is initiated.

2.2 Continuum Damage Constitutive Model

The damage in an elastic-plastic material with hardening manifests itself in two forms: softening of the yield stress and degradation of the elasticity. In order to describe the characteristic stress-strain behavior of the material undergoing damage, a constitutive relation between damaged and intact materials is established by employing internal thermodynamically irreversible damage variables acting as a measure of local failure. Damage initiation is predicted with a similar expression as the yield criterion, but only using parameters α , β and ω corresponding to ultimate strength instead. Once the damage initiation criterion has been reached, material stiffness is assumed to be progressively degraded until enough energy is absorbed for complete failure. Within the framework of Mohr's theory, it seems more reasonable to define the damage variable matrix, $\mathbf{M}^{\text{fp}}(\boldsymbol{\Omega})$, in the fracture plane coordinate system, because the dramatic reduction in load carrying capacity is directly caused on the fracture plane. According to the principle of strain equivalence, a general relationship between the nominal stress and the effective stress of material with micro cracks can be defined

$$\bar{\boldsymbol{\sigma}}_{\text{fp}} = \mathbf{M}^{\text{fp}}(\boldsymbol{\Omega}) : \boldsymbol{\sigma}_{\text{fp}} \tag{10}$$

where for the isotropic damage model, $\mathbf{M}^{\text{fp}}(\boldsymbol{\Omega}) = (1/\omega)\mathbf{I}$, $\omega = 1 - d$. The density of complementary energy for the damaged material based on the principle of energy equivalence is then written as

$$W_d = \frac{1}{2} \bar{\boldsymbol{\sigma}}_{\text{fp}} : \mathbf{D}_{\text{fp}}^{e,-1} : \bar{\boldsymbol{\sigma}}_{\text{fp}} = \frac{1}{2} \boldsymbol{\sigma}_{\text{fp}} : \mathbf{D}_{\text{fp}}^{d,-1} : \boldsymbol{\sigma}_{\text{fp}} \quad (11)$$

here $\mathbf{D}_{\text{fp}}^d = \mathbf{M}_{\text{fp}}^{-1} \mathbf{D}_{\text{fp}}^e \mathbf{M}_{\text{fp}}^{-T}$ is the damaged stiffness tensor defined on the fracture plane. By using coordinate transformation matrix \mathbf{T} , the above relationship could be further expressed under the material principal plane,

$$\mathbf{D}^d = \mathbf{T} \mathbf{M}_{\text{fp}}^{-1} (\mathbf{T}^{-1} \mathbf{D}^e \mathbf{T}^{-T}) \mathbf{M}_{\text{fp}}^{-T} \mathbf{T} = (1-d)^2 \mathbf{D}^e \quad (12)$$

Assuming a linear evolution law with a negative slope results in following internal damage variable

$$d^I = \max \left\{ 0, \min \left\{ 1 - \frac{\varepsilon_{\text{eq},I}^f (\varepsilon_{\text{eq},I} - \varepsilon_{\text{eq},I}^0)}{\varepsilon_{\text{eq},I} (\varepsilon_{\text{eq},I}^f - \varepsilon_{\text{eq},I}^0)} \right\} \right\}, \quad I \in (t, c) \quad (13)$$

where $\varepsilon_{\text{eq},I}$, $\varepsilon_{\text{eq},I}^0$ and $\varepsilon_{\text{eq},I}^f$ are the equivalent strains at the current phase, damage initiation and final failure, respectively. Damage irreversibility is accounted for with the functional form 'max'. Specifically for the general multi-axial stress conditions,

$$d = 1 - (1 - d^t)(1 - d^c) \quad (14)$$

The interaction of stresses acting on the fracture plane (σ_n and τ_n) is the dominant factor driving fracture, so the equivalent stress and corresponding strain are

$$\sigma_{\text{eq}} = \sqrt{\langle \sigma_n \rangle^2 + \tau_n^2}, \quad \varepsilon_{\text{eq}} = \sqrt{\langle \varepsilon_n \rangle^2 + \gamma_n^2} \quad (15)$$

A strong mesh dependency is introduced due to strain localization, such that the energy dissipated decreases upon mesh refinement. Thus, to reduce the sensitivity to the mesh size, the softening response after damage initiation is proposed according to the dissipated fracture energy G_c that is given as

$$G_c = \int_{\varepsilon_{\text{eq}}^0}^{\varepsilon_{\text{eq}}^f} L_c \sigma_{\text{eq}} d\varepsilon_{\text{eq}} = \frac{1}{2} L_c \sigma_{\text{eq}}^0 (\varepsilon_{\text{eq}}^f - \varepsilon_{\text{eq}}^0) \quad (16)$$

where L_c is the characteristic length to keep a constant energy release rate per unit area of the crack; σ_{eq}^0 denotes the equivalent stress at damage initiation. With the definition of a quadratic interaction function for considering the strain energy release density in the mix-mode case, $\varepsilon_{\text{eq}}^f$ then can be derived as

$$\varepsilon_{\text{eq}}^f = \varepsilon_{\text{eq}}^0 + \frac{2}{L_c} \left[\left(\frac{\beta_\sigma \sigma_n}{G_{2c}} \right)^2 + \left(\frac{\beta_\tau \tau_n}{G_{12c}} \right)^2 \right]^{-1/2}, \quad \beta_\sigma = \frac{\langle \varepsilon_n \rangle}{\varepsilon_{\text{eq}}}, \quad \beta_\tau = \frac{\gamma_n}{\varepsilon_{\text{eq}}} \quad (17)$$

in which G_{2c} and G_{12c} are the critical fracture energy release rates corresponding to tension and shear, respectively.

2.3 Integration Algorithm and Consistent Tangent Stiffness

A stress return mapping algorithm is applied in the fully implicit integration scheme of elasto-plasticity constitutive equations. Given a pseudo-time interval Δt , the values of all internal variables at the end of the interval, t_{n+1} , needs to be found according to the known values at the beginning of a time step t_n . In plasticity, the current state of an elementary material volume may be completely characterized by the total strain, plastic strain and additional yield and hardening variables, of which basic equations include the linear relation between the stress tensor and the elastic strain, the consistency condition defined by the yield surface, the

flow rule and equivalent plastic strain associated with the gradient of a plastic potential function

$$\boldsymbol{\sigma}_{n+1} = \mathbf{D}^e : \boldsymbol{\varepsilon}_{n+1}^e = (\boldsymbol{\sigma}_n + \mathbf{D}^e : \Delta \boldsymbol{\varepsilon}) - \mathbf{D}^e : \Delta \boldsymbol{\varepsilon}_{n+1}^p = \boldsymbol{\sigma}_{n+1}^{\text{tr}} - \mathbf{D}^e : \Delta \boldsymbol{\varepsilon}_{n+1}^p \quad (18)$$

$$f(\boldsymbol{\sigma}_{n+1}, \boldsymbol{\varepsilon}_{e,n+1}^p) = f_E(\sigma_{V,n+1}, \sqrt{J_{2,n+1}}, \theta_{\sigma,n+1}, \varphi_{n+1}, \boldsymbol{\varepsilon}_{e,n+1}^p) - 1 = 0 \quad (19)$$

$$\Delta \boldsymbol{\varepsilon}^p = \Delta \lambda \frac{\partial g}{\partial \boldsymbol{\sigma}} = \Delta \lambda \mathbf{b}(\boldsymbol{\sigma}) \quad (20)$$

$$\Delta \boldsymbol{\varepsilon}_c^p = \Delta \lambda B(\boldsymbol{\sigma}) \quad (21)$$

In the above, \mathbf{D}^e represents the standard isotropic elastic stiffness matrix; $\boldsymbol{\sigma}_{n+1}^{\text{tr}}$ denotes the trial stress tensor; the non-negative scalar parameter, $\Delta \lambda$, customarily denotes the rate of the plastic multiplier; $\boldsymbol{\varepsilon}_{n+1}^p$ and $\boldsymbol{\varepsilon}_{e,n+1}^p$ are the plastic strain tensor and equivalent plastic strain at t_{n+1} respectively. Since there may not be any exact solution, an iterative Newton-Raphson procedure is employed to iteratively obtain the solution of nonlinear simultaneous equations. The system of nonlinear equations yields to the following expression of the increment of plastic multiplier rate

$$\delta \lambda = \frac{f - \mathbf{U} \mathbf{Q}^{-1} \mathbf{D}^e \mathbf{M} + \frac{\partial f}{\partial \boldsymbol{\varepsilon}_c^p} N}{\mathbf{U} \mathbf{Q}^{-1} \mathbf{D}^e \mathbf{b} - \frac{\partial f}{\partial \boldsymbol{\varepsilon}_c^p} B} \quad (22)$$

$$\text{with } \mathbf{Q}^{-1} = \left(\mathbf{I} + \Delta \lambda \mathbf{D}^e \frac{\partial \mathbf{b}}{\partial \boldsymbol{\sigma}} \right)^{-1}, \quad \mathbf{U} = \frac{\partial f}{\partial \boldsymbol{\sigma}} + \Delta \lambda \frac{\partial f}{\partial \boldsymbol{\varepsilon}_c^p} \frac{\partial B}{\partial \boldsymbol{\sigma}} \quad (23)$$

where \mathbf{I} is the identity matrix. Substitution of $\delta \lambda$ back leads to the results of $\Delta \boldsymbol{\sigma}$, $\Delta \boldsymbol{\varepsilon}^p$ and $\Delta \boldsymbol{\varepsilon}_c^p$. Afterwards improved approximations are able to be evaluated at the next iteration, and the iterative process is stopped if the residuals f^{k+1} and $\Delta \boldsymbol{\sigma}^{k+1}$ are negligible.

The determination of the material consistent tangent stiffness or Jacobian is required in the implicit iterative procedure to minimize the force residual and achieve convergence. Typically in the plastic regime, the Jacobian, J_p , can be deduced by differentiating the stress-strain relationship as well as the consistency condition. So that the final formula of the Jacobian matrix is provided by

$$J_p = \frac{\partial \boldsymbol{\sigma}}{\partial \boldsymbol{\varepsilon}} = \mathbf{Q}^{-1} \mathbf{D}^e - \frac{\mathbf{Q}^{-1} \mathbf{D}^e \mathbf{b} \mathbf{U} \mathbf{Q}^{-1} \mathbf{D}^e}{\mathbf{U} \mathbf{Q}^{-1} \mathbf{D}^e \mathbf{b} - \frac{\partial f}{\partial \boldsymbol{\varepsilon}_c^p} B} \quad (24)$$

When damage is activated, the damage Jacobian, J_d , is adopted instead as the plastic strain tensors no longer changes. Eventually, it writes

$$J_d = \mathbf{D}^d + \frac{\partial \mathbf{D}^d}{\partial \boldsymbol{\sigma}} (\boldsymbol{\varepsilon} - \boldsymbol{\varepsilon}_f^p) \quad (25)$$

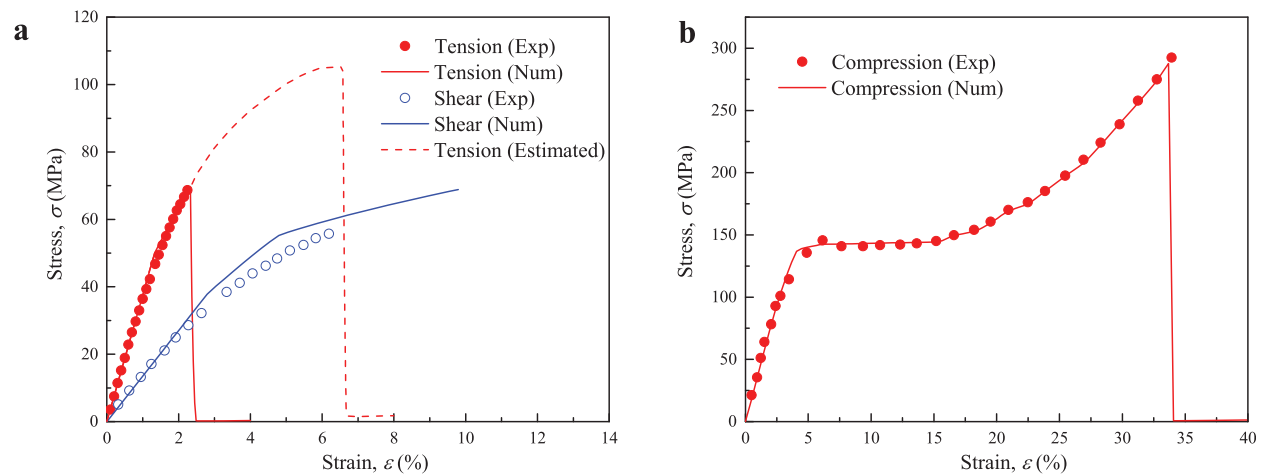
3 Calibration and Validation of Plasticity Model

In order to validate the matrix constitutive model described in the previous section, the experimental results from Sun's work [15] are used with regard to the epoxy matrix XPR-0273-31 subjected to uniaxial tension, compression and torsion. A summary of elastic material properties is listed in Tab. 1 below.

Table 1: Elastic materials properties for fibers and matrix used in RVEs

	Elastic modulus /GPa		Shear modulus /GPa		Poisson's ratio	
Fibers	E_{11}	E_{22} (E_{33})	G_{12} (G_{13})	G_{23}	ν_{12}	
	245	19.8	29.191	5.922	0.28	
Matrix	E_m		G_m		ν_m	ν_p
	3.73		1.351		0.38	0.3

The stress-strain responses measured by standard specimens at the macroscale level and those predicted by numerical simulations are shown in Fig. 2 for three loading scenarios. Perfect consistency is achieved between measured and predicted results of tension and compression, whereas the predicted shear stress somewhat higher than the one recorded experimentally. The reason is that the shear stress herein is actually fitted by the isotropic hardening law presented in Section 2.1. As captured by the numerical prediction, the matrix exhibits high shear nonlinearity, and it does not reach failure even for very high values of plastic straining. Overall, the proposed model captures well all basic characteristics of highly non-linear mechanical responses of the matrix.

**Figure 2:** Comparisons of numerical and experimental results of stress-strain responses for (a) tension and torsion, (b) compression

While accurate simulations of the micromechanical properties of RVEs have to rely on the actual values of the matrix properties, the direct use of experimental data that is measured by conventional macroscopic specimens is worthy of further discussion. The presence of internal defects, such as void cavitation, will result in a strong size effect in tensile strength [16-18]. Experimental observation has demonstrated that the average tensile fracture strength obtained from fiber-shaped matrix specimens is about 55% higher than that measured from the macroscopic test methods on dog-bone specimens [16]. In other words, when taking the strength measured by macroscopic specimens as the input parameters of the RVE model, a hypothesis is accordingly made that every matrix element contains as many critical defects as in a much larger macroscopic specimen. Considering that the typical volume of the resin filled inter-fiber region is extremely smaller, such hypothesis may severely underestimate and not reproduce the real strength during analysis [19]. Consequently, one other kind of the ultimate fracture strength of the epoxy matrix are

presented herein to study the size effect. Due to the lack of experimental data obtained by means of experimental nanomechanics, the ultimate strength at the microscale level, corresponding to the typical size of resin-filled inter-fiber volume in the UD composite, is made an increase in 1.55 times (a conservative estimation according to [17]) higher than experimental data measured by macroscopic methods. As shown in Fig. 2a, the microscopic nonlinear responses are simplified according to similar tendencies of representative scaled stress-strain curves extracted from Fiedler et al. [16].

4 Micromechanical Evaluation on RVE Model

4.1 Finite Element Discretization

The mechanical responses of the plies are obtained by means of the periodic RVE technique. 3D cuboid RVEs of the composite microstructures are generated having multiple randomly distributed fibers embedded inside the polymeric matrix. To represent essential macro-scale mechanical characteristics without increasing computational costs significantly, the width and thickness of RVEs are limited to $12R_f$ and R_f respectively, where R_f is the fiber radius assumed to have identical value. The properties for reinforcing AKSACA carbon fibers with identical diameter of $7\ \mu\text{m}$ and volume fraction of 51.4% are taken from [15], as listed in Tab. 1. Both fibers and matrix are meshed using 8-node linear hexahedral reduced integration elements (C3D8R) with hourglass control, while 8-node cohesive elements (COH3D8) are adopted to represent the interfaces [21-24]. The average mesh size of the three phases is set to be $0.1R_f$, resulting in approximately 200,000 elements contained in each RVE model. To meet the requirement of periodicity and continuity in the deformation and stresses at adjacent cell boundaries, a unified periodical boundary condition (PBC) is applied for the unit cell instead of uniform homogenous boundary conditions [25, 26]. The homogenized mechanical responses are able to be computed by integrating and averaging the stress or strain over the RVE volume, i.e., the volumetric homogenization approach described in detail in [20].

Indeed, the difference in fiber distribution could affect the fracture strength of the RVE. When referring to random fiber array of microstructures, it can be inferred that the inter-fiber spacing may play a role in the failure behavior of composites under mechanical loading. The best way is to establish the RVE model strictly in accordance with the fiber distribution and geometry at the fracture location of the experimental specimen. However, the location of damage initiation is non-accessible before imposing loads, and meanwhile the cut sections of the specimen is hardly to be observed without destruction by current inspection methods. Fortunately, parametric studies conducted by Melro et al. [20] and He et al. [21] have shown that the influence of fiber distribution is limited on the macro-scale tensile strength (within the maximum error of 10%). Therefore a kind of distribution of fibers is randomly selected by the author.

4.2 Influence of Matrix and Fiber-Matrix Interface Mechanical Properties in Homogenized Failure Strength

In order to fully assess the role played by matrix damage and interfacial debonding in macroscopic transverse tensile strength, plots of homogenized stress-engineering strain curves, predicted by different input properties given in the previous Section 3, are compared with experimental measurements. The numerical predictions are from the RVEs, respectively with and without considering interfacial damage. The fracture properties (strength and toughness) of cohesive elements used here are chosen to be equal to the initial values listed in Tab. 2.

Table 2: Material properties of interface [10, 20]

$K_n(K_s)$ (MPa/mm)	t_n^0 (MPa)	$t_s^0(t_t^0)$ (MPa)	G_{Ic} (N/mm)	$G_{IIc}(G_{IIIc})$ (N/mm)
108	50	70	0.002	0.006

The effect of matrix strength gained at different scale levels on the transverse tension behavior is illustrated in Fig. 3. As expected the matrix strength significantly affects the responses of the RVEs, with the homogenized tensile strength increasing as the tensile strength of the epoxy matrix is increased. All curves show that tensile fractures happen at relatively lower stresses and strains, causing more than 30% reductions in the stress levels sustainable by a pure matrix. A similar reduction was also reported in [13, 20]. The elastic regimes of all the curves are nearly superposed, and divergences occur at slight yield stages which are obviously found in the curves with higher matrix strength. Interestingly even without regard to the occurrence of debonding between fibers and matrix, the predicted failure strength of 43.7 MPa given by the macromechanical properties is about 29.6% lower than the average experimental value of 62.1 MPa. But from a point of view of rationality, the predictions, like those from the other two higher inputs, should be equal or greater. This phenomenon questions the accuracy of the results in the references that use properties directly obtained from macroscopic standard specimens, of which the volume is much larger than the real size of the matrix between fibers. The size effect of matrix strength may not be neglected as a result of flaw sensitivity.

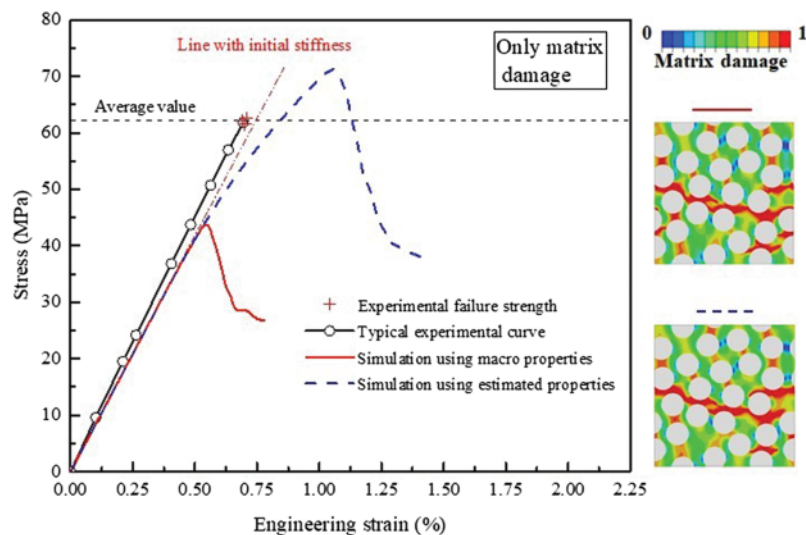


Figure 3: Comparisons of numerical and experimental results of stress-strain curves with damage only activated in the matrix

If the interfacial damage is taken into account, the curves from all the RVEs exhibit nearly uniform trends, as shown in Fig. 4. They behave slightly nonlinear until the appearance of a sudden stress drop, implying that the inelastic deformation only occurs in a small region before the homogenized strength reaches the maximum value. In contrast to numerical results by using matrix properties measured on standard specimens, substantial difference of both stress-strain curves and damage contours can be observed between predictions with and without considering interfacial failure (marked with the blue lines in Figs. 3 and 4) when using microscale related properties. It suggests that interfacial debonding, rather than matrix cracking, becomes the governing mechanism in the damage scenario induced by transverse tension. The stress and strain levels of RVEs are obviously lower than the pure matrix, owing to the stress triaxiality generated by the existence of the fibers.

4.3 Calibrating Fracture Properties of Cohesive Element

Therefore, the specific values of interface fracture properties, i.e., the bond strength and the critical energy release rate, no doubt affect the ultimate macro strength on the premise of using higher micro

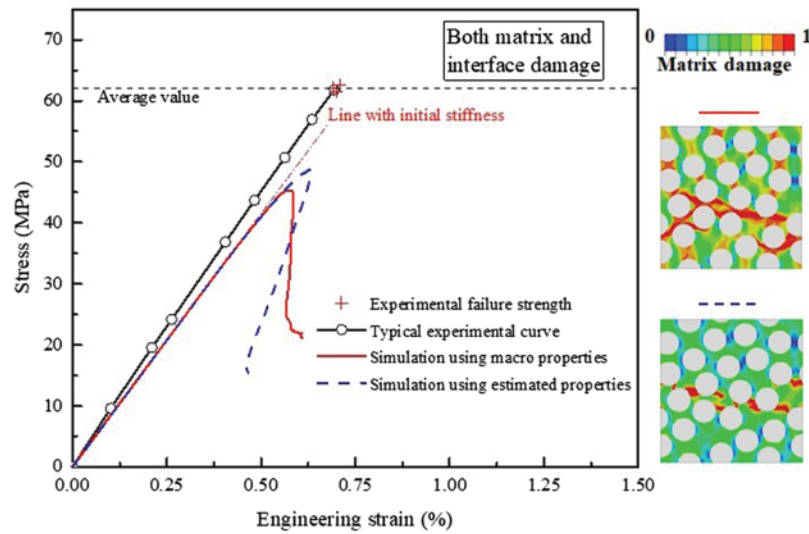


Figure 4: Comparisons of numerical and experimental results of stress-strain curves with damage activated at the fiber-matrix interfaces and in the matrix

properties of the epoxy matrix. As discussed previously, it has demonstrated that the cohesive elements, with application of interfacial properties that are widely selected by recent references, would make incorrectly predictions. In order to give appropriate values, a zoom factor is proposed to represent the linear relationship between the calibrated one and the initial default. A parametrical analysis is carried out by a periodic RVE model containing one single fiber, assuming that only one interfacial parameter is varied when rest parameters remain equal to the initial defaults. To avoid interference from matrix damage, damage is only activated in the cohesive elements, while the material remained in the elastic loading regime. The strength corresponding to the complete stiffness degradation (namely initial debonding) of a cohesive element is recorded and normalized with the failure strength obtained by the initial values. The numerically predicted results of Fig. 5 clearly reveal that the mode I interfacial properties t_n^0 and G_{Ic}

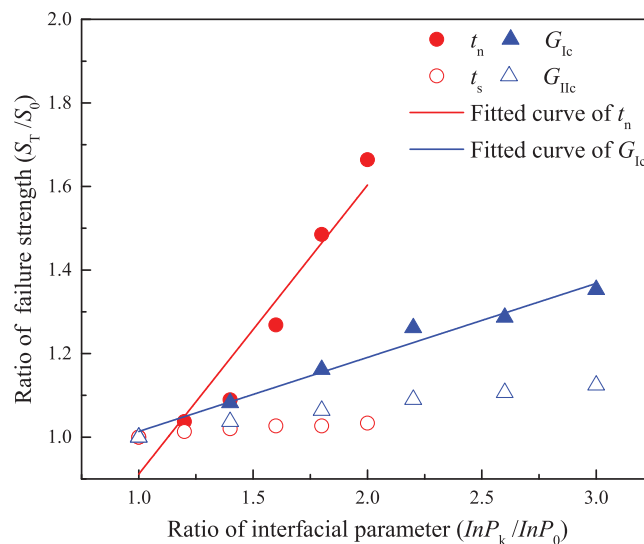


Figure 5: Predictions of nominal failure strength by varying interfacial parameters respectively under transverse tension

exhibit significant effects on transverse tensile strength, and the values of mode I fracture can be further calibrated through an inverse approach depending on data from uniaxial tension experiments. Therefore with the fitted curves, the values of zoom factors corresponding to t_n^0 and G_{Ic} are about 1.4 and 2.0, respectively.

4.4 Experimental Verification for RVEs

The homogenized stress-engineering strain curves obtained by tensile experiments and those predicted by the RVE models are compared in the graphs of Figs. 6 and 7. Good agreement is achieved between measured and predicted results of stress. The specific phenomenon of a macroscopic fracture band, generated by interfacial debonding and microscopic matrix cracks, is successfully captured. The inter-fiber fracture band with rough surface develops nearly perpendicular to the loading direction through the entire thickness of a RVE, which is consistent with experimental observations.

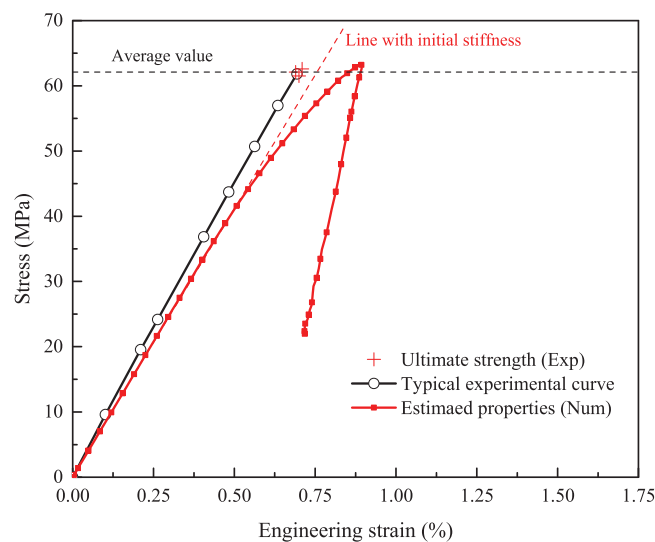


Figure 6: Comparison between experimental and numerical homogenized stress-engineering strain curves under transverse tension

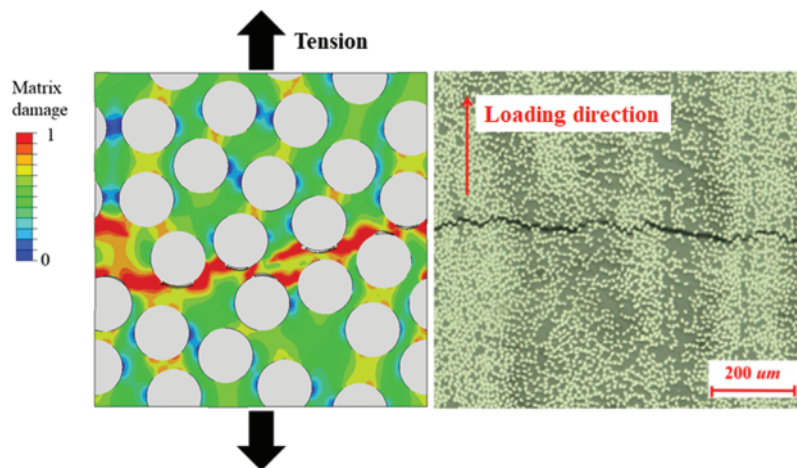


Figure 7: Comparison between damage images obtained by optical microscope [15] and FEA at the end of the numerical simulations

5 Discussions

5.1 Failure Mechanisms Under Transverse Tension

The initiation and propagation mechanisms of both matrix cracking and fiber-matrix interface debonding, which dominate the composite's transverse strength at the macroscale level, are studied by means of computational micromechanics. Fig. 8 gives the predicted damage scenario in the composite material subjected to uniaxial tension.

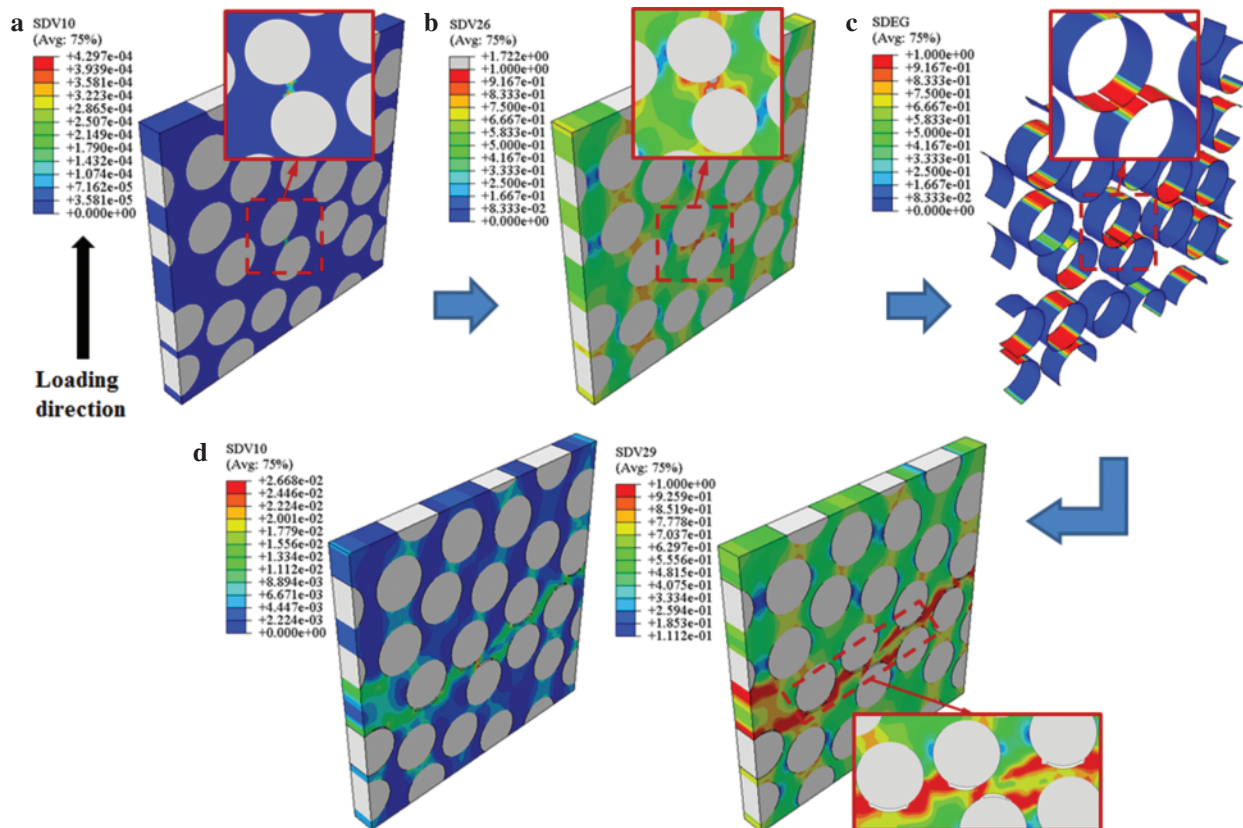


Figure 8: Contour plots of (a) equivalent plastic strain ε_c^p at the macro-strain $\varepsilon = 0.34\%$, (b) matrix tensile failure at $\varepsilon = 0.88\%$, (c) fiber-matrix debonding at $\varepsilon = 0.89\%$ and (d) ultimate fracture morphology, with respect to transverse tension

In the initial stage of the transverse tension, as shown in Fig. 8a, when the macro engineering strain reaches approximately 0.34%, the initiation of plastic deformation firstly occurs in the matrix closely adjacent to the fiber-matrix interface. Due to the fiber cluster along the loading direction, higher stress concentrations in this region will lead to premature yielding in comparison to the case of pure matrix under uniaxial tension. The plastic deformation is found to be away from the resin-rich regions and increases dramatically, resulting in the initiation of matrix tensile failure near the pole of the fiber. The phenomenon can be clearly seen from a partial enlarged drawing in Fig. 8b. As the load is instantaneously transferred from the damaged matrix elements to the intact interfaces, complete debonding of the fiber-matrix interface is triggered next to the elements where matrix damage has initiated or even propagated (see Fig. 8c). At the meantime, the homogenized stress-strain curve experiences a sudden tension strength drop. In a similar fashion, more extensive matrix damage and

interfacial cracks successively appear at the vicinity of fiber, and along with the increase of the plastic strains in the matrix, interfacial cracks are coalesced with neighbors by the propagation of matrix cracking. Ultimately, a crack band, perpendicular to the loading axis, develops through the entire RVE (Fig. 8d), meaning thoroughgoing fracture in practice.

5.2 Fracture Plane Angles Corresponding to Scales of Constituent and Ply Levels

The specific values of fracture plane angles φ_{fp} , which is at the scale of a constituent level and closely related to stress states at damage initiation of matrix elements, is available to be identified by the modified yield criterion based on Mohr's failure plane theory. Distribution of fracture plane angles is presented in the following Fig. 9.

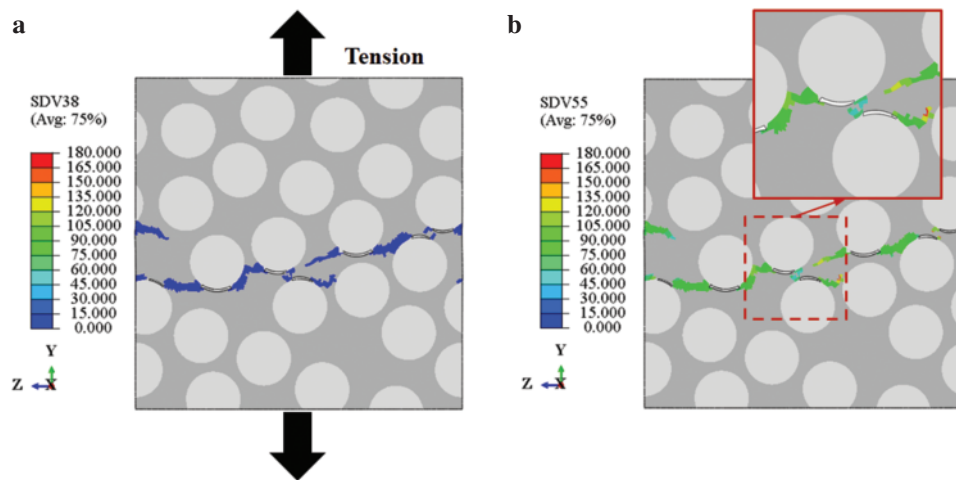


Figure 9: (a) Distribution of fracture plane angles φ_{fp} with respect to minimum principal stress σ_3^p and (b) orientation of σ_3^p with respect to the loading direction, in the RVE subjected to transverse tension

Figure 9a gives the angle distribution in the RVE under transverse tension. Note that the so called fracture plane angle here is defined as the angle between the matrix fracture plane and minimum principal stress σ_3^p . In the region of the crack band, its fracture plane angles are predicted with values of around 0° , obviously demonstrating that the positive normal stress acting on the actual fracture plane is the dominant stress causing the critical matrix cracking during tension. However, since the triaxial stress states of the matrix are caused by the existence of the fibers with random distributions, the orientation of σ_3^p in each matrix element is not exactly the same with respect to the loading direction. More specifically, as shown in Fig. 9b, the orientation of σ_3^p near the fiber pole varies from 45° to 70° , while it is equal to 90° for the rest of most failure elements. Thus, the actual fracture plane of the matrix at the scale of a fiber level is not always perpendicular to the loading axis at all, especially those existing in the vicinity of fibers, implying jagged surfaces of the macroscopic crack band from the macroscopic point of view (at the scale of a ply level).

In regard to transverse tensile loading, it is important to recognize that matrix tensile failure and fiber-matrix interfacial debonding are the only two failure modes of constituent materials, and therefore the transverse tensile strength of a UD composite depends on the competition between above-mentioned failure modes. As directly using measurements at the scale of the ply level fails to obtain reasonable results, the predictions with application of conservatively higher matrix strength, corresponding to the scale of the fiber level, still proves a crucial role played by the interfacial fracture. Although matrix

tensile failure firstly initiates near the fiber, the strength drop is related to the complete debonding of the fiber-matrix interfaces. The interfacial strength and toughness (more specifically refer to Mode I fracture properties t_n^0 and G_{Ic}) determine the mechanical performance of UD composites subjected to transverse tensile loading.

6 Conclusions

In this paper, a phenomenological-based micromechanical method comprising a novel constitutive model, developed to describe elasto-plastic with isotropic damage behaviors of epoxy matrix materials, and a CZM model, employed to estimate interfacial fracture, is proposed to investigate the failure mechanisms of UD CFRP composites subjected to transverse tension. Numerical and experimental evaluation demonstrates that the proposed constitutive model has a high degree of capability in capturing elasto-plastic responses of the matrix materials.

When directly using matrix properties that are measured in standard specimens at the macroscale level (ply scale level) to characterize mechanical behaviors of the inter-fiber matrix at the microscale level (constituent scale level), obvious underestimation exists in predictions as a result of earlier failure and lower homogenized strength.

The inter-fiber fracture band at the ply level develops nearly perpendicular to the loading direction through the entire thickness of a RVE. However, the distribution of matrix fracture plane angles at the scale of constituent level indicates that under transverse tension, the surface of the macroscopic crack band, running perpendicular to the loading axis, is not smooth. Due to the high stress triaxiality, the fracture plane angles of the matrix at the vicinity of fibers varies from 20° to 45° with respect to the plane perpendicular to the loading axis, despite they are equal to 0° for the rest of most failure material elements.

Acknowledgement: The authors sincerely thank for the support by National Science Foundation for Young Scientists of China under Grant [No. 11802116].

References

1. Puck, A., Kopp, J., Knops, M. (2002). Guidelines for the determination of the parameters in Puck's action plane strength criterion. *Composites Science and Technology*, 62(3), 371–378. DOI 10.1016/S0266-3538(01)00202-0.
2. Hinton, M. J., Kaddour, A. S., Soden, P. D. (2004). *Failure Criteria in Fibre Reinforced Polymer Composites: The World-Wide Failure Exercise*. Oxford: Elsevier Ltd.
3. Kaddour, A. S., Hinton, M. J. (2013). Maturity of 3D failure criteria for fibre-reinforced composites: comparison between theories and experiments: Part B of WWFE-II. *Journal of Composite Materials*, 47(6–7), 925–966. DOI 10.1177/0021998313478710.
4. Knops, M. (2008). *Analysis of Failure in Fiber Polymer Laminates: The Theory of Alfred Puck*. Berlin: Springer.
5. Li, N., Gu, J. F., Chen, P. H. (2018). Fracture plane based failure criteria for fiber-reinforced composites under three-dimensional stress state. *Composite Structures*, 204, 466–474. DOI 10.1016/j.compstruct.2018.07.103.
6. Gonzalez, C., LLorca, J. (2007). Mechanical behavior of unidirectional fiber-reinforced polymers under transverse compression: microscopic mechanisms and modeling. *Composites Science and Technology*, 67(13), 2795–2806. DOI 10.1016/j.compscitech.2007.02.001.
7. Totry, E., Gonzalez, C., LLorca, J. (2008). Failure locus of fiber-reinforced composites under transverse compression and out-of-plane shear. *Composites Science and Technology*, 68(4), 829–839. DOI 10.1016/j.compscitech.2007.08.023.
8. Totry, E., Molina-Aldareguia, J. M., Gonzalez, C., LLorca, J. (2010). Effect of fiber, matrix and interface properties on the in-plane shear deformation of carbon-fiber reinforced composites. *Composites Science and Technology*, 70(6), 970–980. DOI 10.1016/j.compscitech.2010.02.014.

9. Vaughan, T. J., McCarthy, C. T. (2011). A micromechanical study on the effect of intra-ply properties on transverse shear fracture in fibre reinforced composites. *Composites: Part A*, 42(9), 1217–1228. DOI 10.1016/j.compositesa.2011.05.004.
10. Vaughan, T. J., McCarthy, C. T. (2011). Micromechanical modelling of the transverse damage behaviour in fibre reinforced composites. *Composites Science and Technology*, 71(3), 388–396. DOI 10.1016/j.compscitech.2010.12.006.
11. Soni, G., Singh, R., Mitra, M., Falzon, B. G. (2014). Modelling matrix damage and fibre-matrix interfacial decohesion in composite laminates via a multi-fibre multi-layer representative volume element (M^2RVE). *International Journal of Solids and Structures*, 51(2), 449–461. DOI 10.1016/j.ijsolstr.2013.10.018.
12. Melro, A. R., Camanho, P. P., Pires, F., Pinho, S. T. (2013). Micromechanical analysis of polymer composites reinforced by unidirectional fibers: Part I-constitutive modeling. *International Journal of Solids and Structures*, 50(11–12), 1897–1905. DOI 10.1016/j.ijsolstr.2013.02.009.
13. Ullah, Z., Kaczmarczyk, L., Pearce, C. J. (2017). Three-dimensional nonlinear micro/meso-mechanical response of the fiber-reinforced polymer composites. *Composite Structures*, 161, 204–214. DOI 10.1016/j.compstruct.2016.11.059.
14. Gu, J. F., Chen, P. H. (2018). A failure criterion for isotropic materials based on Mohr's failure plane theory. *Mechanics Research Communications*, 87, 1–6. DOI 10.1016/j.mechrescom.2017.11.008.
15. Sun, Q. P., Meng, Z. X., Zhou, G. W., Lin, S. P., Kang, H. et al. (2018). Multi-scale computational analysis of unidirectional carbon fiber reinforced polymer composites under various loading conditions. *Composite Structures*, 196, 30–43. DOI 10.1016/j.compstruct.2018.05.025.
16. Fiedler, B., Hojo, M., Ochiai, S., Schulte, K., Ando, M. (2001). Failure behavior of an epoxy matrix under different kinds of static loading. *Composites Science and Technology*, 61(11), 1615–1624. DOI 10.1016/S0266-3538(01)00057-4.
17. Hobbiebrunken, T., Fiedler, B., Hojo, M., Tanaka, M. (2007). Experimental determination of the true epoxy resin strength using micro-scaled specimens. *Composites Part A*, 38(3), 814–818. DOI 10.1016/j.compositesa.2006.08.006.
18. Wisnom, M. R. (1999). Size effects in the testing of fibre-composite materials. *Composites Science and Technology*, 59(13), 1937–1957. DOI 10.1016/S0266-3538(99)00053-6.
19. Chevalier, J., Camanho, P. P., Lani, F., Pardoën, T. (2019). Multi-scale characterization and modelling of the transverse compression response of unidirectional carbon fiber reinforced epoxy. *Composite Structures*, 209, 160–176. DOI 10.1016/j.compstruct.2018.10.076.
20. Melro, A., Camanho, P. P., Pires, F. A., Pinho, S. T. (2013). Micromechanical analysis of polymer composites reinforced by unidirectional fibres: Part II-micromechanical analyses. *International Journal of Solids and Structures*, 50(11–12), 1906–1915. DOI 10.1016/j.ijsolstr.2013.02.007.
21. He, C. W., Ge, J. R., Qi, D. X., Chen, Y., Liang, J. et al. (2019). A multiscale elasto-plastic damage model for the nonlinear behavior of 3D braided composites. *Composites Science and Technology*, 171, 21–33. DOI 10.1016/j.compscitech.2018.12.003.
22. Arteiro, A., Catalanotti, G., Melro, A. R., Linde, P., Camanho, P. P. (2015). Micro-mechanical analysis of the effect of ply thickness on the transverse compressive strength of polymer composites. *Composites Part A*, 79, 127–137. DOI 10.1016/j.compositesa.2015.09.015.
23. Arteiro, A., Catalanotti, G., Melro, A. R., Linde, P., Camanho, P. P. (2014). Micro-mechanical analysis of the in situ effect in polymer composite laminates. *Composite Structures*, 116, 827–840. DOI 10.1016/j.compstruct.2014.06.014.
24. Canal, L. P., Gonzalez, C., Segurado, J., LLorca, J. (2012). Intraply fracture of fiber-reinforced composites: Microscopic mechanisms and modeling. *Composites Science and Technology*, 72(11), 1223–1232. DOI 10.1016/j.compscitech.2012.04.008.
25. Li, S., Wongsto, A. (2004). Unit cells for micromechanical analyses of particle-reinforced composites. *Mechanics of Materials*, 36(7), 543–572. DOI 10.1016/S0167-6636(03)00062-0.
26. Xia, Z., Zhang, Y., Ellyin, F. (2003). A unified periodical boundary conditions for representative volume elements of composites and applications. *International Journal of Solids and Structures*, 40(8), 1907–1921. DOI 10.1016/S0020-7683(03)00024-6.